Mechatronics and Intelligent Transportation Systems
https://www.acadlore.com/journals/MITS

MCSSA-CNN-BiLSTM-Attention Model-Based Prediction and Compensation Control for Rebound in Ship Hull Outer Plate Processing

Dongxu Liu[1, 2], Xin Liu[1, 2, 3*], Yang Zhang[1, 2], Pengfei Hou[1, 2], Haiwen Yuan[4]

[1] School of Ship and Port Engineering, Shandong Jiaotong University, 264209 Weihai, China
[2] Weihai Institute of Marine Information Science and Technology, 264200 Weihai, China
[3] Shandong Premium Boating Technology Ltd., 253300 Dezhou, China
[4] Killer Whale Intelligent Technology (Shandong) Co., 264201 Weihai, China

[*] Correspondence: Xin Liu (axinzaixian@163.com)

Received: 09-15-2025 **Revised:** 10-28-2025 **Accepted:** 11-14-2025

Citation: D. X. Liu, X. Lin, Y. Zhang, P. F. Hou, and H. W. Yuan, "MCSSA-CNN-BiLSTM-attention model-based prediction and compensation control for rebound in ship hull outer plate processing," *Mechatron. Intell Transp. Syst.*, vol. 4, no. 4, pp. 210–231, 2025. https://doi.org/10.56578/mits040404.

Abstract: This study proposed a novel pin-level dynamic compensation strategy to combat the critical challenge of springback in the three-dimensional numerically controlled bending of ship hull plates. A collaborative prediction model combining convolutional and bidirectional recurrent networks (CNN-BiLSTM) was optimized using an improved metaheuristic algorithm, the Modified Sparrow Search Algorithm (MCSSA), to achieve millimeter-level precision in springback compensation. Based on the 225-pin independent control architecture, the system enabled real-time compensation with millisecond-level response ($\leq$ 50 ms) on standard industrial computing hardware, to overcome the limitations of conventionally fixed compensation methods. The optimized algorithm enhanced global search capability, population diversity, and convergence efficiency, hence yielding a prediction accuracy of RMSE = 4.41×10^{-5} mm. The integrated spatiotemporal learning framework effectively combined feature extraction, sequential modeling, and critical region emphasis, to achieve a test-set R^2 of 0.969. Industrial validation of the SKWB-1600 system demonstrated significant improvements in traditional stepwise approximation methods: (i) Post-compensation forming errors were reduced to 0.13–0.26 mm with a 47–62% improvement; and (ii) Curvature errors in high-stress zones were maintained within $\pm$ 0.02 mm, thus forming iterations decreased by 42% and energy consumption reduced by 35%. This certified pin-level dynamic compensation solution provides a new methodology for forming precision of complex curved ship hull plates under industrial conditions and establishes a technical paradigm for manufacturing related components requiring high precision and efficiency.

Keywords: Springback prediction; MCSSA; BiLSTM; Finite element; Dynamic compensation; Parametric simulation

1 Introduction

Plate bending machines play an essential role in the high-precision forming of complex curved hull plates, replacing traditional flame-bending through Computer Numerical Control (CNC) adjustable mold systems. Despite technical advancement, springback caused by material elastoplasticity remains a major obstacle to achieving dimensional accuracy. Current approaches integrate finite element simulation, neural network prediction, and real-time control to compensate for springback, hence underscoring a shift toward intelligent and precision-aware forming technologies.

Most research on springback in sheet metal forming has focused on V- or U-bending configurations [1–3], with studies emphasizing the influence of material properties, process parameters, and tool geometry [4]. The finite element method (FEM) is well-established for springback prediction [5], with key factors affecting accuracy, such as tool design, process conditions, material models, and numerical settings [3, 6]. For example, Slota and Jurčišin [7] developed a finite element (FE) based model for air bending of transformation–induced plasticity (TRIP) and advanced high-strength steels (AHSS), while Wasif et al. [8] used variance analysis to identify sheet thickness and bend angle as dominant factors of high-strength steel springback. Uemori et al. [9] employed U-bent hat sections to validate hardening models that capture transient Bauschinger behavior, which is critical for accurate springback prediction [3–5].

Although recent object detection algorithms, such as YOLOv7 and YOLOv6, have shown strong performance in general industrial vision tasks [10, 11], they are unsuitable for springback prediction due to their architectural focus on discrete bounding-box detection rather than continuous regression of physical parameters like displacement or stress, which is essential for springback quantification. Their high computational cost [12] and trade-off between inference speed and precision [13] limit their use in real-time forming applications where millimeter-level accuracy is required.

Various strategies have been proposed to mitigate springback. The studies [14–17] introduced reconfigurable discrete molds for adaptive control. And the studies [18–20] developed asymmetric press-head layouts to improve forming efficiency. Liang [21] characterized material springback nonlinearity using multi-point press experiments, whereas Xu [22] optimized process parameters via neural networks. Zhang [23] reduced errors to millimeter scale using a whale-algorithm-optimized (WOA) Generalized Regression Neural Network (GRNN) model, and Wei [24] automated compensation with Genetic Algorithm optimized Back Propagation (GA-BP) networks. Inamdar et al. [25] further improved model robustness through expanded training datasets.

In summary, despite these contributions, existing methods exhibited three principal limitations that this work aimed to address: (1) inadequate modeling of stress-field coupling under multi-press-head synergy [26]; (2) poor adaptability to resource-constrained hardware, such as edge computing devices deployed on unmanned vessels or within resource-limited industrial controllers [27]; and (3) a persistent trade-off between computational efficiency and prediction accuracy in real-time deployment. There is an apparent need for an integrated framework that combines high-fidelity simulation, lightweight yet accurate modeling, and real-time compensation control specifically designed for industrial environments.

To address these gaps, this study proposed an integrated innovation framework comprising three key advances: (1) an Ansys Parametric Design Language (APDL) LS-DYNA explicit-implicit co-simulation model that captures nonlinear coupling among load, thickness, and material properties; (2) a hybrid Modified Sparrow Search Algorithm Convolutional and Bidirectional Recurrent (MCSSA-CNN-BiLSTM) Attention Network that balances spatial feature extraction, temporal sequence modeling, and computational efficiency, optimized via modified sparrow search with sine-cosine operators, Cauchy mutation, and elite opposition-based learning; and (3) a closed-loop control system that incorporates 3D laser scanning and real-time press-head adjustment at the individual pin level to achieve millisecond response and significant improvement in compensation accuracy on standard industrial hardware, e.g., NVIDIA Quadro series graphic processing units (GPU).

Together, these three advances form a novel approach that overcomes the limitations of current methods. A robust and scalable solution was provided for springback compensation in industrial ship hull forming, with potential applicability in other domains requiring high-precision sheet metal forming.

2 Construction and Validation of ASSAM-CNN-Billet-Attention Fusion Model

2.1 Design of the MCSSA Optimization Algorithm

The sparrow search algorithm constitutes an intelligent optimization method inspired by the collective foraging and predator evasion behaviors of sparrow flocks [28]. It stratifies the population into three functional roles: discoverers employ broad environmental perception to pioneer food source pathfinding; joiners implement following strategies to exploit located resources; and scouts continuously monitor environmental threats while activating collective anti-predator mechanisms. This tripartite structural dynamics accurately simulate survival strategies in complex ecosystems: discoverers conduct pathfinding expeditions, joiners intensively utilize identified resources, and scouts maintain exploration-exploitation equilibrium through risk alerts, hence granting the algorithm simultaneous spatial exploration breadth and optimization refinement depth during solution space traversal [29]. Consequently, the algorithm achieves convergence-secured optimal solution targeting 20% scout vigilance sustaining adaptive stability, and establishing computational equivalence between biological survival tactics and multidimensional optimization mechanics for enhanced global convergence security in engineering applications [30–32].

1) Position Update Formula for Discoverers:

$$X_i^t = \begin{cases} X_1^t \cdot \exp\left(\dfrac{-i}{\alpha I_{\max}}\right), & R_2 \le ST \\ X_i^t + Q \cdot L, & \text{others} \end{cases} \tag{1}$$

This formula governs the position update of the "discoverer" sparrows in the MCSSA algorithm. It embodies the exploration-exploitation trade-off. When the alert value R_2 is below the safety threshold ST, sparrows perform localized exploitation around the current best solution (exponential decay term). Conversely, when threatened, they relocate randomly (Gaussian distributed term "$Q \cdot L$") to explore new regions of the search space, thus preventing premature convergence. This stochastic behavior is crucial for optimally navigating the high-dimensional parameter space of the neural network (e.g., learning rates and number of units) to minimize prediction error.

Herein, t denotes the current iteration count, T represents the maximum iteration count, X_i^t indicates the position information of the i-th sparrow at iteration t, i signifies the spatial dimension,α is a random number within [0, 1],

$R_2 \in [0, 1]$ denotes the alert threshold, $ST \in [0.5, 1]$ indicates the safety threshold, Q is a random number subject to normal distribution, and L represents a row vector with conditionality matching the search space, where every element equals to 1.

2) Position Update Formula for Joiners:

$$X_i^{t+1} = \begin{cases} Q \cdot \exp\left(\dfrac{X_{\text{worst}}^t - X_i^t}{t^2}\right), & i > \dfrac{n}{2} \\ X_b^{t+1} + \left|X_i^t - X_b^{t+1}\right| \cdot A^+ \cdot L, & \text{others} \end{cases} \tag{2}$$

This rule models the follower behavior of joiner sparrows. Sparrows with lower fitness ($i > \frac{n}{2}$) are in a hungry state and perform a random walk (first case) to explore new areas for food. Others (second case) compete for the discoverer's previous best position (X_b^{t+1}), with the matrix operation $A^+ \cdot L$ defining a specific search direction around it. These balances directed following and random exploration.

X_{worst}^t denotes the current global worst position; $X(t)$ represents the best position occupied by the discoverers; N signifies the population size; $A^+ = A^T \left(A^T A^T\right)^{-1}$, A represents a row vector of conditionality d with elements randomly assigned as either 1 or -1, and A^+ indicates the transpose of A [24].

3) Position Update Formula for Scouts:

$$X_i^{t+1} = \begin{cases} X_{\text{best}}^t + \beta \left|X_i^t - X_{\text{worst}}^t\right|, & f_i > f_v \\ X_i^t + k \left(\dfrac{\left|X_i^t - X_{\text{worst}}^t\right|}{f_i - f_v}\right), & f_i = f_v \end{cases} \tag{3}$$

This governs the anti-predator response of scouts. Sparrows sensing danger (first case, $f_i > f_v$) flee towards the perceived safest area (X_{best}^t). Sparrows at the edge of the group (second case, $f_i > f_v$) move closer to others for safety. This critical risk-awareness mechanism enhances population survival and prevents convergence in poor regions (ϵ is a small constant for numerical stability).

X_{best} denotes the current global best position; $\alpha \sim N(0, 1)$ represents the step-size regulator, a random number drawn from a standard normal distribution (mean 0, variance 1); $k \in$ [-1, 1] signifies the movement direction of sparrows, also modulating step-size magnitude.

The traditional sparrow search algorithm tends to fall into local optimum and has limited convergence accuracy in complex imitation problems, mainly due to its excessive randomness and insufficient population diversity in its position update strategy. In order to solve this problem, a multi-strategy collaborative improvement of the sparrow algorithm is proposed, which enhances the global exploration and local exploitation capabilities through a three-stage strategy:

1) Sine-Cosine Oscillation Perturbation Strategy:

Implement Sine Cosine Algorithm (SCA) updates on Discoverers' positions:

$$X_i = \begin{cases} X_i + r_1' \cdot \sin r_2 \cdot \left|r_3 \cdot X_{best} - X_i\right|, R_2 < ST \\ X_i + r_1' \cdot \cos r_2 \cdot \left|r_3 \cdot X_{best} - X_i\right|, R_2 > ST \end{cases} \tag{4}$$

This strategy introduces an oscillatory perturbation around the current best solution (X_{best}). The sine and cosine functions create a periodic fluctuation, enabling the algorithm to explore both inward and outward regions relative to X_{best}. This is particularly effective in escaping local optima and thoroughly scanning promising areas in the search domain, which corresponds to fine-tuning the network parameters for a more accurate and generalizable springback prediction model.

Within this formulation, $r_1' \in [0, 2\pi]$ is a random number governing sparrows' movement distance, while $r_3 \in [0, 2\pi]$ is a stochastic parameter modulating the elite individual's influence on subsequent sparrow positioning.

2) Cauchy Mutation Perturbation Strategy:

Apply Cauchy mutation operator to Joiners' positions:

$$X_i = X_{best}(t) + \text{cauchy}(0, 1) \cdot X_{best}(t) \tag{5}$$

Cauchy mutation is applied to joiners to increase population diversity and escape local optima. The standard Cauchy distribution cauchy (0,1) has a heavier tail than the Gaussian distribution, meaning it has a higher probability of generating larger perturbations or 'jumps'. Adding this scaled random value to the current best solution ($X_{best}(t)$) allows the algorithm to aggressively explore distant areas in the search space that might be overlooked by other strategies, potentially leading to the discovery of a superior global optimum for the prediction task.

In this formulation, cauchy (0,1) denotes the standard Cauchy distribution function.

3) Dynamic Elite Opposition-Based Learning:

Construct opposition-based solutions for elite individuals to enhance population diversity:

$$X_i = m\left(lb_i(t) + ub_i(t)\right) - X_i \tag{6}$$

This strategy generates the opposite position (X_i^{new}) of the current elite individual (X_i^{old}) within the dynamically updated bounds $[lb_i(t), lb_i(t)]$ of the search space. The core idea is that if the current solution is not near the optimum, its opposite might be closer to it. By simultaneously evaluating both the current and opposite solutions, the algorithm doubles the search efficiency and increases the probability of finding a better region. The dynamic bounds prevent wasted evaluations in unreasonably large or already explored areas.

In the formulation m is a random number within [0, 1], termed the elite reverse coefficient; lb and ub denote the upper and lower boundaries of the individual's feasible solution space.

Algorithm Convergence Verification:

As shown in Figure 1, in the imitation experiments of the multi-peak test function F3 (Astringent function), the MCSSA demonstrates significant advantages. It converges at 300 generations, which is a 40% speed-up compared to the 500 generations required by the traditional SSA; and the final adaptation value reaches 5.21×10^{-7}, which is an improvement of 2 orders of magnitude compared to SSA. The standard deviation of 30 independent experiments is only 18% of the SSA, which verifies the overall improvement of the algorithm in convergence speed, accuracy, and robustness.

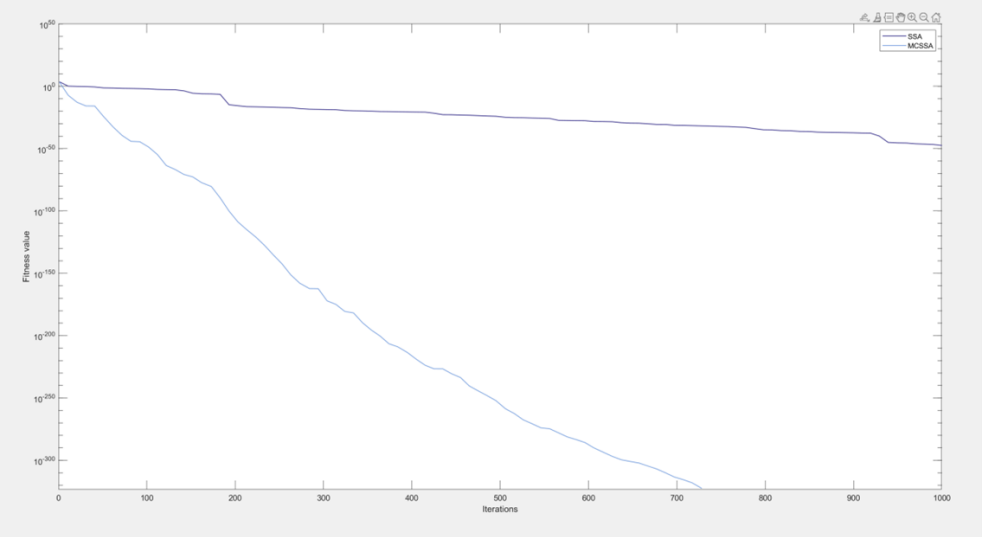

Figure 1. Semi-logarithmic coordinate plot

To quantitatively evaluate the effectiveness of the proposed modifications such as sine-cosine oscillation, Cauchy mutation, and elite opposition-based learning in the MCSSA algorithm, a comparative ablation study was conducted. The search performance of the standard SSA, SSA with only Cauchy mutation (SSA-C), SSA with only sine-cosine strategy (SSA-SC), and the full MCSSA was tested on the CEC2005 benchmark function F3 (Ackley function) over 1,000 iterations. The results, summarized in Table 1, demonstrated the contribution of each strategy to the convergence precision and stability of the algorithm.

Table 1. Ablation study of the performance of different SSA variants

Algorithm Variant	Convergence Iterations	Best Fitness Value	RMSE (Mean $\pm$ Std)
Standard SSA	850	3.72×10^{-3}	$(6.24 \times 10^{-3}) \pm (2.81 \times 10^{-3})$
SSA with Cauchy	720	2.15×10^{-4}	$(4.98 \times 10^{-4}) \pm (1.76 \times 10^{-4})$
SSA with Sine-Cosine	650	9.87×10^{-5}	$(3.11 \times 10^{-4}) \pm (1.02 \times 10^{-4})$
Full MCSSA	500	5.21×10^{-7}	$(4.41 \times 10^{-5}) \pm (1.12 \times 10^{-5})$

As shown in Table 1, the full MCSSA algorithm achieved superior performance, converging in nearly half of the iterations required by the standard SSA and reaching a significantly better fitness value. The Cauchy mutation (SSA-C) greatly enhanced the ability to escape local minima, as evidenced by the improved fitness. The sine-cosine strategy (SSA-SC) effectively accelerated the convergence rate. The integration of all three strategies in the MCSSA

synergistically combined these advantages, resulting in the fastest convergence, the highest precision, and the most stable performance (lowest standard deviation), which is critical for reliably optimizing the neural network parameters for springback prediction.

2.2 Architecture of the CNN-Billet-Attention Model

The model is designed for the task of ship outer plate rebound prediction and consists of an input layer, a convolutional layer (CNN), an attention mechanism layer (SE module), a bi-directional long and short-term memory network (Billet), and a fully connected output layer. Its core is to mine the spatial features and sequence dependencies of rebound data through multi-module collaboration, and the specific structure is as follows:

(1) Input Layer

The input to the model is the deformation characteristic matrices collected from 4,226 spatial nodes under 77 loading conditions. To prepare for the data, the raw springback datasets first underwent standardized processing via min-max scaling to normalize load magnitudes and plate thicknesses within the [0,1] range. The processed data was then partitioned into training and test sets, to ensure multimodal heterogeneous data compatibility for model input.

(2) Convolutional Layer (CNN) with Activation

Spatiotemporal features in springback deformation fields were extracted by 1×1 convolutional kernels (initial layer: 32 channels) through stride = 1 sliding-window operations. ReLU activation enforced nonlinear transformation to amplify discriminative feature signatures while suppressing gradient dissipation risks during error back propagation cycles.

The architecture of the CNN feature extractor employed is illustrated in Figure 2. It delineates the hierarchical data flow from the input feature sequence, through the convolutional and pooling layers where local spatiotemporal patterns are captured and condensed, to the fully-connected layers that integrate these features for higher-order representation. The highlighted convolution and pooling kernels visually demonstrate the core operations of localized feature extraction and dimensionality reduction; these are fundamental to processing the data of complex deformation field.

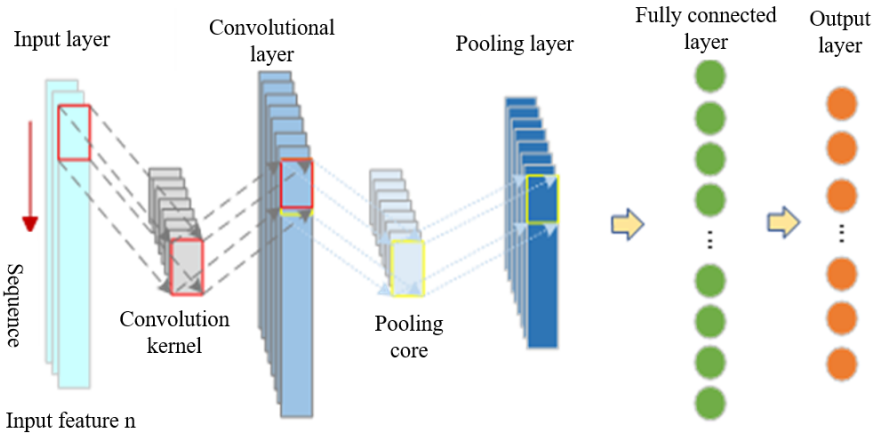

Figure 2. Diagram of CNN network structure

(3) Attention Mechanism Layer

This approach employed an innovative squeeze-excitation-recalibration structure to optimize feature processing. To begin with, it efficiently compressed feature map information using global average pooling, thereby reducing redundant data. Subsequently, the mechanism, through fully connected layers incorporating Rectified Linear Unit (ReLU) and sigmoid activation functions, deeply learned and outputted channel-specific weighting values. To conclude the process, feature recalibration was performed by multiplying the learned weights with the original features, which adaptively enhanced the significance of critical channel features to improve the representation capacity and generalization accuracy of the model.

The detailed data flow of the Squeeze-and-Excitation (SE) block is depicted in Figure 3. The schematic diagram explicitly traces the transformation of the input feature maps x ($H' \times W' \times C'$) through the squeeze (Fsq: global average pooling) and excitation (Fex: two FC layers with ReLU and Sigmoid) operations, culminating in the generation of channel-wise weights. These weights were then scaled (Fscale) with the original features to produce the recalibrated output $\hat{x}$. This visualization underscores the ability of the mechanism to model channel interdependencies and amplify informative features critical for accurate springback prediction.

(4) Bidirectional Long Short-Term Memory Network (BiLSTM)

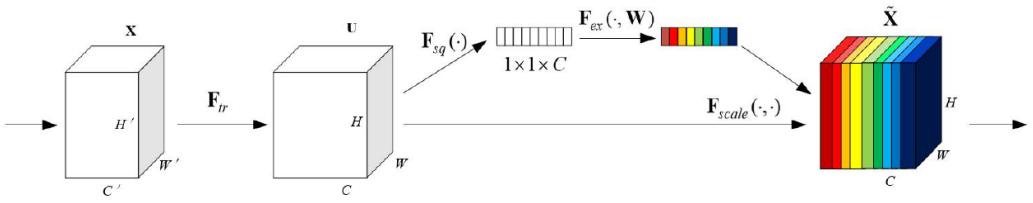

Figure 3. Diagram of the structure of SE mechanism network

This approach utilized a bidirectional LSTM structure for data processing. The forward LSTM processes data chronologically in the forward direction to capture historical dependencies, while the backward LSTM processes data in reverse chronological order to incorporate future insights. Ultimately, the hidden states from both directions were concatenated to generate a unified feature vector that encapsulates comprehensive contextual information. This method fully leverages the bidirectional temporal dependencies within the data to deliver a more comprehensive feature representation.

Figure 4 provides a clear visualization of the bidirectional processing mechanism of the BiLSTM network. It shows the parallel forward (path A) and backward (path B) LSTM units processing the input sequence ($\mathrm{X_{t-1}}, \mathrm{X_t}, \mathrm{X_{t+1}}$) in opposite temporal directions. The concatenation of their respective hidden states (h_t) at each time step forms the comprehensive contextual output (y_t), which incorporates information from both past and future states relative to the current time step. This architectural insight is crucial for understanding how the model captures the complex temporal evolution of stress and strain during the plate bending process.

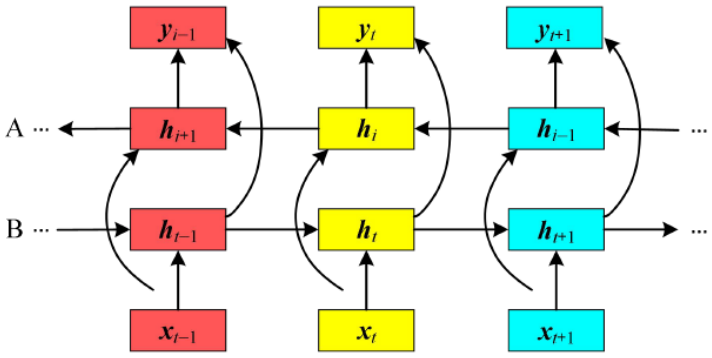

Figure 4. Diagram of the BiLSTM network structure

The hidden state h_t of the BiLSTM network at time step t integrates information from both forward $\overrightarrow{h_t}$ and backward $\overleftarrow{h}_t$ passes:

$$\overrightarrow{h_t} = \overrightarrow{LSTM}\left(\overrightarrow{h_{t-1}}, x_t, \overrightarrow{c_{t-1}}\right), t \in [1,\ \mathrm{T}] \tag{7}$$

where, the LSTM unit computes:

$$i_t = \sigma(W_{xi}x_t + W_{hi}\overrightarrow{h_{t-1}} + b_i) \quad \text{(Input gate)}$$

$$f_t = \sigma(W_{xf}x_t + W_{hf}\overrightarrow{h_{t-1}} + b_f) \quad \text{(Forget gate)}$$

$$o_t = \sigma(W_{xo}x_t + W_{ho}\overrightarrow{h_{t-1}} + b_o) \quad \text{(Output gate)}$$

$$\tilde{c}_t = \tanh(W_{xc}x_t + W_{hc}\overrightarrow{h_{t-1}} + b_c) \quad \text{(Candidate cell state)}$$

$$\overrightarrow{c_t} = f_t \odot \overrightarrow{c_{t-1}} + i_t \odot \tilde{c}_t \quad \text{(Current cell state)}$$

$$\overrightarrow{h_t} = o_t \odot \tanh(\overrightarrow{c_t}) \quad \text{(Current Hidden state)}$$

$$\overleftarrow{h_t} = \overleftarrow{LSTM}\left(\overleftarrow{h_{t-1}}, x_t, \overleftarrow{c_{t-1}}\right), t \in [\ \mathrm{T}, 1] \tag{8}$$

where, the LSTM unit computes:

$$i'_t = \sigma(W'_{xi}x_t + W'_{hi}\overleftarrow{h_{t+1}} + b'_i) \quad \text{(Input gate)}$$

$$f'_t = \sigma(W'_{xf}x_t + W'_{hf}\overleftarrow{h_{t+1}} + b'_f) \quad \text{(Forget gate)}$$

$$o'_t = \sigma(W'_{xo}x_t + W'_{ho}\overleftarrow{h_{t+1}} + b'_o) \quad \text{(Output gate)}$$

$$\widetilde{c'_t} = \tanh(W'_{xc}x_t + W'_{hc}\overleftarrow{h_{t+1}} + b'_c) \quad \text{(Candidate cell state)}$$

$$\overleftarrow{c_t} = f'_t \odot \overleftarrow{c_{t+1}} + i'_t \odot \tilde{c'_t} \quad \text{(Current cell state)}$$

$$\overleftarrow{h_t} = o'_t \odot \tanh(\overleftarrow{c_t}) \quad \text{(Current hidden state)}$$

$$H_t = \left[\overrightarrow{h_t}, \overleftarrow{h_t}\right] \tag{9}$$

This represents the final hidden state of the BiLSTM layer, formed by concatenating the forward ($\overrightarrow{h_t}$) and backward ($\overleftarrow{h_t}$) passes. This concatenated state H_t encapsulates the complete contextual information of the input sequence up to time t. In the context of springback prediction, this allows the model to understand how past and future load steps collectively influence the stress and strain at the current moment, hence capturing the temporal evolution of the material's deformation behavior.

Function: Modeling bidirectional long-term dependencies of springback variation with load changes.

(5) Fully-Connected Layer and Output Layer

The fully-connected layer integrates and maps the higher-order features of the BiLSTM output to the prediction dimension, and finally outputs the continuous rebound volume prediction through the regression layer.

2.3 Fusion Model Optimization and Analysis of the Experiments

(1) Model Optimization Framework This study proposed an MCSSA-integrated optimization framework (see Figure 5), where deep fusion between the MCSSA and the CNN-BiLSTM-Attention (CBA) model enables adaptive hyperparameter tuning of key structural parameters. The framework constructs a search space with sparrow position vectors encoding critical configurations, such as CNN channel counts and the BiLSTM hidden units, targeting minimization of the test set Root Mean Square Error (RMSE). A phased optimization mechanism operates through three synchronized strategies: global exploration expands search scope using a sine-cosine-based discoverer update strategy to circumvent local optima; local refinement employs a follower update mechanism enhanced by Cauchy mutation to intensify exploitation through heavy-tailed perturbations; concurrent elite retention directly inherits the top 10% of individuals per generation to accelerate convergence, hence collectively achieving systematic performance enhancement of the predictive model.

(2) Comparison of Experimental Results

The proposed MCSSA-CBA fusion model demonstrated outstanding performances across extensive experimental datasets in Table 2. Leveraging a multi-strategy optimization approach, the model achieved significantly shorter convergence times and enhanced computational efficiency compared to conventional methods. Test results confirmed superior prediction accuracy over standalone neural network architectures, particularly those exhibiting stronger adaptability when processing complex curved-surface data.

Ablation studies verified that the integrated attention mechanism critically improved prediction precision for high-curvature regions. Computational latency remained constrained at low levels, fully satisfying requirements of real-time industrial control. This intelligent and efficient springback prediction approach effectively reduces processing cycles while elevating production efficiency.

(3) Visualization Analysis

1) Predicted-Actual Fit Performance

As illustrated in Figure 6, the curves of predicted and actual value demonstrate high congruence on the test set, exhibiting distinctive spatial distribution characteristics. In high-springback central regions, the maximum absolute prediction error of the model was merely 0.035 mm, constituting less than 3.5% of the tolerance threshold of classification societies. In low-springback edge zones, errors remained consistently controlled within $\pm$ 0.01 mm. Figure 7 further quantifies global fitting precision through scatter plots, revealing a test set coefficient of determination R^2 of 0.969, with 95% of sample points distributed within the Y = X $\pm$ 0.02 mm confidence interval. The fitted line slope of 0.981 confirmed negligible systematic bias, thus fully satisfying precision forming requirements for ship hull plates.

2) Error Distribution and Stability

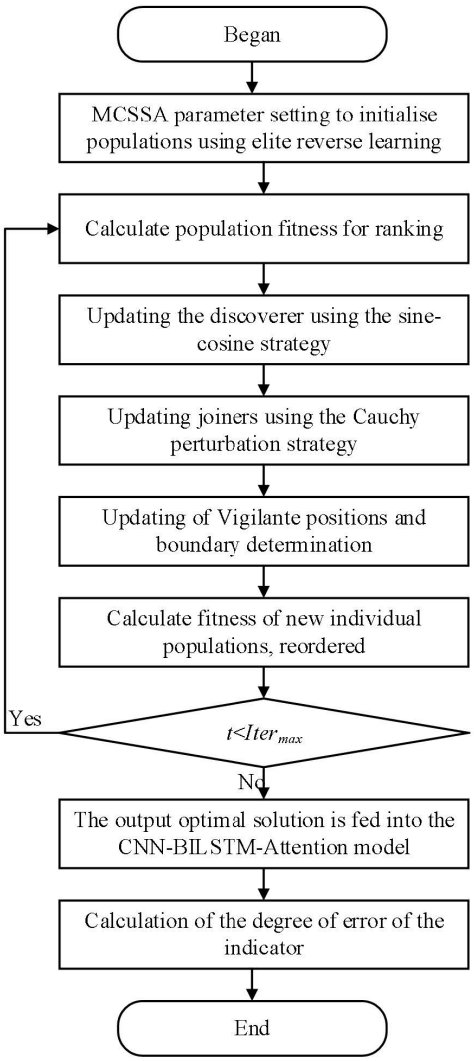

Figure 5. Architecture of the MCSSA-CBA integration

Table 2. Comparison of metrics for five models

Norm	MCSSA-CBA	CNN-BILSTM-Attention	CNN-LSTM-Attention	SSAELMAN	ELMAN
MAE	4.2349×10^{-5} mm	5.4429×10^{-5} mm	5.9950×10^{-5} mm	6.0799×10^{-5} mm	6.3428×10^{-5} mm
MSE	2.0905×10^{-9} mm^2	2.6333×10^{-9} mm^2	3.2241×10^{-9} mm^2	3.4422×10^{-9} mm^2	3.9210×10^{-9} mm^2
RMSE	4.5722×10^{-5}	5.1316×10^{-5}	5.6781×10^{-5}	5.8671×10^{-5}	6.2618×10^{-5}
RPD	2.8100	1.3436	1.3874	1.2801	1.0183
MAPE	3.5524	4.6463	4.3944	4.1233	5.1233

The error distribution displayed light-tailed characteristics, with 92.7% of the samples having absolute errors $\leq$ 0.015 mm, which is in line with the 3σ principle. The distribution demonstrated mild right skewing and spiking characteristics (Figure 8), indicating that the model was more sensitive to positive errors. The error fluctuation curve illustrated that the full domain fluctuation amplitude was controlled within $\pm$ 0.04 mm, in which the proportion of mutation points in the curvature mutation region was $< 0.3\%$, and the standard deviation σ = 0.012 mm (Figure 9). This low volatility and the spatial distribution of the error characteristics verified the robustness of the model under complex working conditions, and provided a reliable guarantee for the dynamic compensatory control.

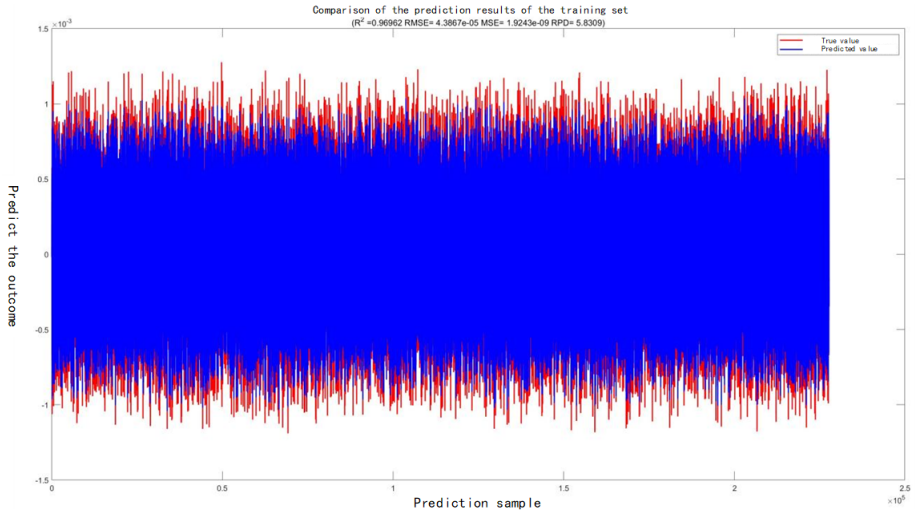

(a)

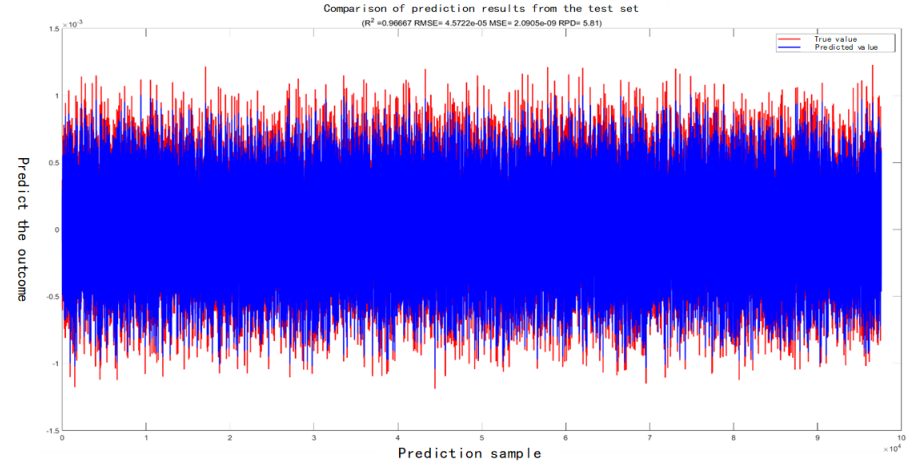

(b)

Figure 6. Plot of: (a) Training set prediction results; (b) Test set prediction results

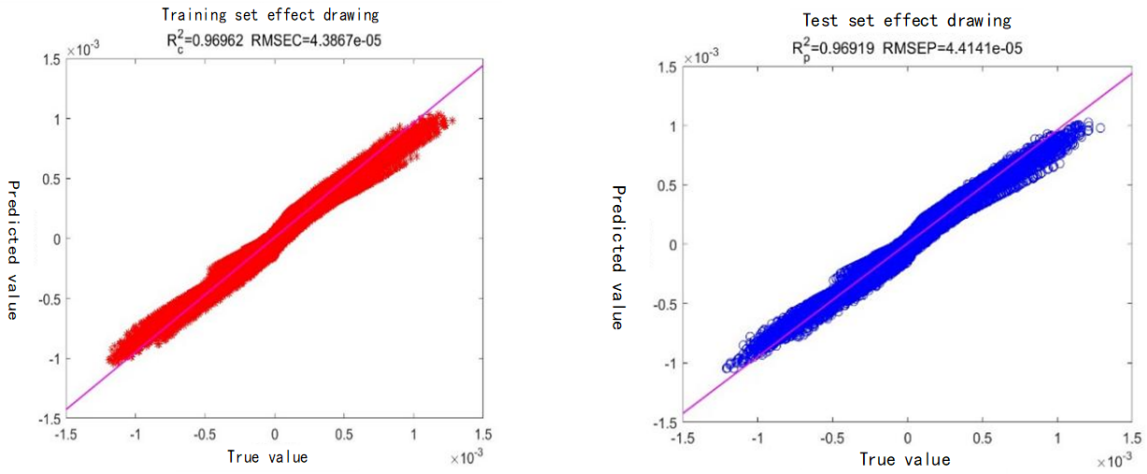

(a) (b)

Figure 7. Plot of: (a) Training set results; (b) Test set results

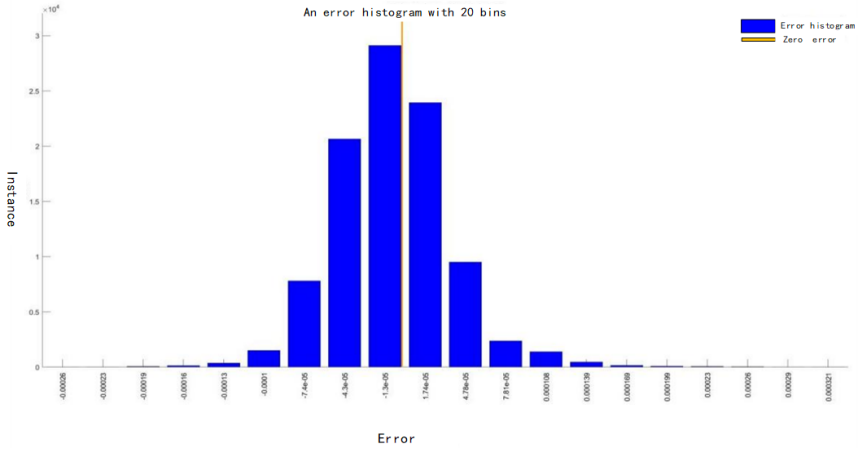

Figure 8. Error histogram of the test set

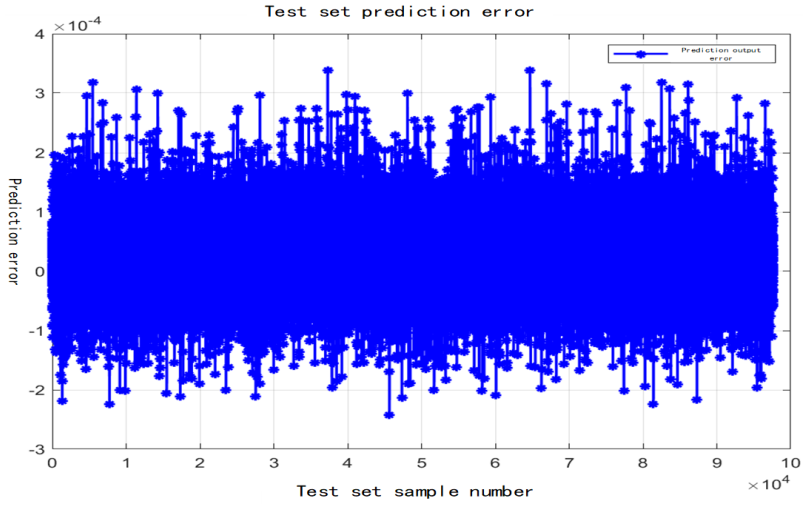

Figure 9. Error fluctuation curve of the test set

3 Generation of Data and Analysis of the Characteristics of Springback

3.1 Ansys Parametric Design Language (APDL) Simulation Modeling

In Figure 10, the finite element model established with APDL for ship plate press forming, employed a 14 × 14 upper die matrix and a 15 × 15 lower die configuration. It simulated the forming process of a 2,000 mm × 1,500 mm Q235 steel plate (E = 206 GPa, v = 0.3).

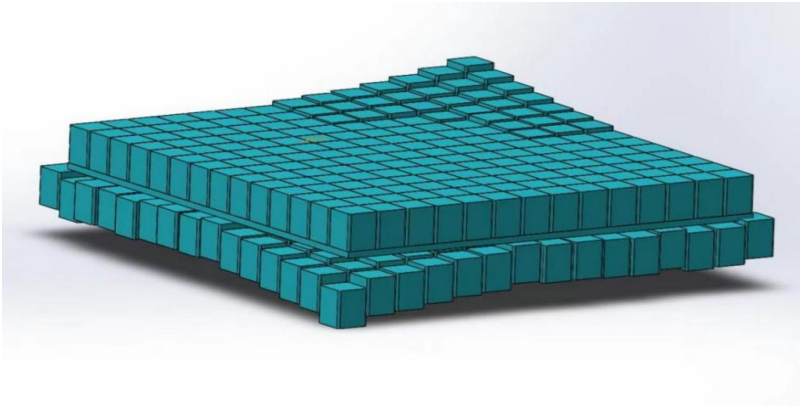

Figure 10. Finite element model of sheet metal stamping

The simulation workflow in Figure 11 employed an explicit-implicit hybrid solution strategy, executed through four key stages: (1) automated generation of a mesh model with 4,226 nodes via APDL parametric scripting; (2) explicit dynamic stamping simulation using LS-DYNA to capture nodal stress-strain fields; (3) transfer of deformation data to the implicit solver via solution restart technology; and (4) analysis of springback with nodal displacement matrix extraction. This parametric modeling approach demonstrated marked advantages over conventional simulations: defining 58 geometric parameters and 22 material parameters enabled batch processing of 77 load cases, while reducing single-simulation runtime to 35% of the duration of traditional methods.

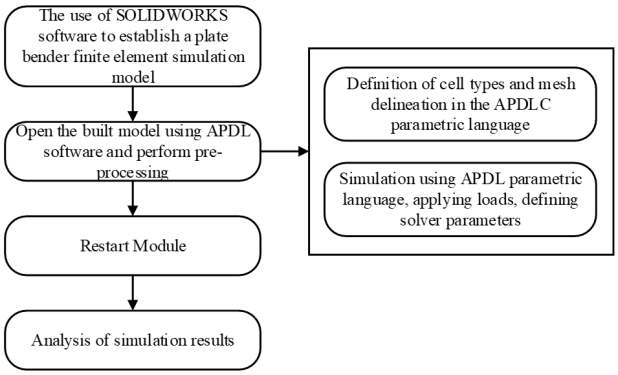

Figure 11. Basic steps for the stamping simulation of sheet metal

3.2 Results of Stamping Simulation

The stamping and forming simulation results revealed the typical stress and strain distribution patterns in the plate during forming. As illustrated in Figure 12, the displacement and stress nephograms depict the geometric morphology of the deformation and the state of stress distribution, respectively, providing fundamental data for subsequent springback analysis. The three-dimensional surface comparison in Figure 13 further highlights the geometric change of the plate before and after springback, with a maximum center displacement of 2.67 mm (for a 5 mm thick plate), showing a significant gradient towards the edges. The local node and height matrices provided in Table 3 offer precise quantitative data on local deformations for model training. These structured datasets not only quantify the stress, strain, and displacement at each node but also elucidate the mechanical response laws of the plate when forming through their spatial distribution patterns.

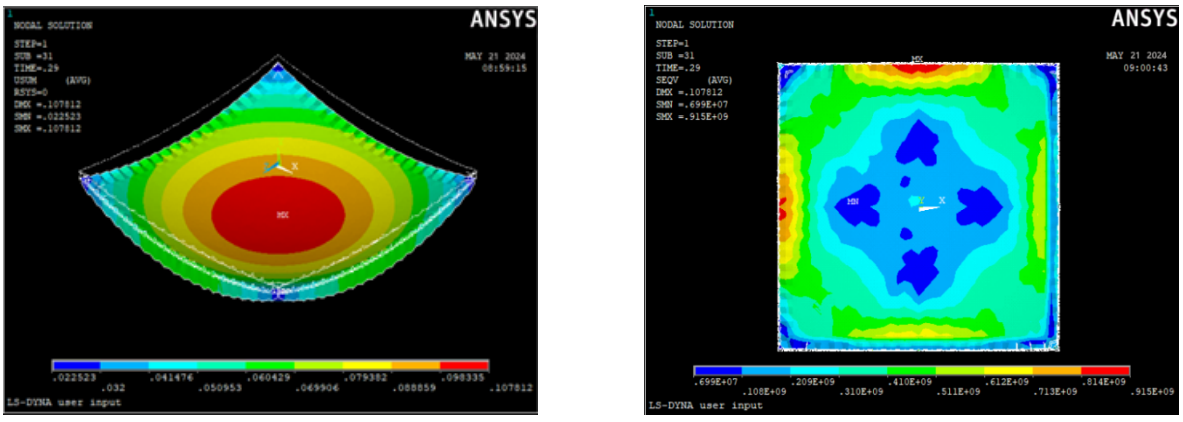

(a) (b)

Figure 12. (a) Displacement contour of the forming process; (b) Stress contour of the forming process

3.3 Analyzing the Data of Springback

The dataset configuration for training the neural network was meticulously designed to ensure both computational tractability and physical comprehensiveness. A selection of 77 loading conditions from 4,000 N to 80,000 N was determined to adequately capture the nonlinear material response across the elastic, yield, and plastic deformation regimes of the Q235 steel plates. This range and resolution prevent under-sampling of the complex load-deformation relationship, a common pitfall that limits the generalizability of a model.

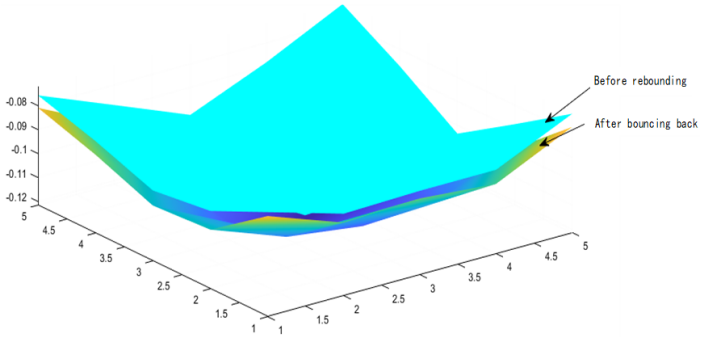

Figure 13. Overall state of the plate before and after Springback

Table 3. Local node matrix and local height matrices before and after Springback

Node Matrix					Height Before Springback (mm)					Height After Springback (mm)				
C1	C2	C3	C4	C5	C1	C2	C3	C4	C5	C1	C2	C3	C4	C5
2	59	69	79	46	-0.0736	-0.0873	-0.0865	-0.0865	-0.0719	-0.0795	-0.0910	-0.0897	-0.0924	-0.0774
440	1629	1639	1649	459	-0.0890	-0.0971	-0.0997	-0.0997	-0.0879	-0.0968	-0.1086	-0.1129	-0.1103	-0.0979
430	1239	1249	1259	469	-0.0921	-0.1021	-0.1215	-0.1133	-0.1035	-0.0984	-0.1140	-0.1215	-0.1183	-0.1073
420	849	859	869	479	-0.0831	-0.0940	-0.1111	-0.1011	-0.0871	-0.0888	-0.1071	-0.1176	-0.1124	-0.0993
206	217	227	237	207	-0.0757	-0.0885	-0.1014	-0.0882	-0.0727	-0.0809	-0.0965	-0.1054	-0.0981	-0.0784

Following a rigorous mesh convergence study, the finite element mesh consisting of 4,226 nodes was adopted. This specific mesh density was identified as the optimal trade-off that guaranteed solution accuracy, with less than 2% deviation from a finer and computationally prohibitive mesh. The trade-off also maintained feasible simulation times for the large number of required runs. This approach ensured the generated data was both accurate and efficient for subsequent model training, hence establishing a robust foundation for the springback prediction task.

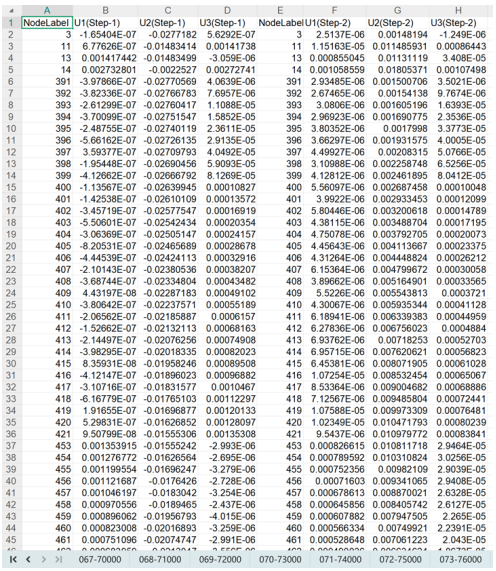

NodeLabel	U1(Step-1)	U2(Step-1)	U3(Step-1)	NodeLabel	U1(Step-2)	U2(Step-2)	U3(Step-2)
3	-1.65404E-07	-0.0277182	5.6292E-07	3	2.5137E-06	0.00148194	-1.249E-06
11	6.77626E-07	-0.01483414	0.00141738	11	1.15163E-05	0.011485931	0.00086443
13	0.001417442	-0.01483499	-3.059E-06	13	0.000855045	0.01131119	3.408E-05
14	0.002732801	-0.0022527	0.00272741	14	0.001058559	0.01805371	0.00107498
391	-3.97866E-07	-0.02770569	4.0639E-06	391	2.93485E-06	0.001500706	3.5021E-06
392	-3.82336E-07	-0.02766783	7.6957E-06	392	2.67465E-06	0.00154138	9.7674E-06
393	-2.61299E-07	-0.02760417	1.1088E-05	393	3.0806E-06	0.001605196	1.6393E-05
394	-3.70099E-07	-0.02751547	1.5852E-05	394	2.96923E-06	0.001690775	2.3536E-05
395	-2.48755E-07	-0.02740119	2.3611E-05	395	3.80352E-06	0.0017998	3.3773E-05
396	-5.66162E-07	-0.02726135	2.9135E-05	396	3.66297E-06	0.001931575	4.0005E-05
397	3.59377E-07	-0.02709793	4.0492E-05	397	4.49927E-06	0.00208315	5.0766E-05
398	-1.95448E-07	-0.02690456	5.9093E-05	398	3.10988E-06	0.002258748	6.5256E-05
399	-4.12662E-07	-0.02666792	8.1269E-05	399	4.12812E-06	0.002461895	8.0412E-05
400	-1.13567E-07	-0.02639945	0.00010827	400	5.56097E-06	0.002687458	0.00010048
401	-1.42538E-07	-0.02610109	0.00013572	401	3.9922E-06	0.002933453	0.00012099
402	-3.45719E-07	-0.02577547	0.00016919	402	5.80446E-06	0.003200618	0.00014789
403	-5.50601E-07	-0.02542434	0.00020354	403	4.38115E-06	0.003488704	0.00017195
404	-3.06369E-07	-0.02505147	0.00024157	404	4.75078E-06	0.003792705	0.00020073
405	-8.20531E-07	-0.02465689	0.00028678	405	4.45643E-06	0.004113667	0.00023375
406	-4.44539E-07	-0.02424113	0.00032916	406	4.31264E-06	0.004448824	0.00026212
407	-2.10143E-07	-0.02380536	0.00038207	407	6.15364E-06	0.004799672	0.00030058
408	-3.68744E-07	-0.02334804	0.00043482	408	3.89662E-06	0.005164901	0.00033565
409	4.43197E-08	-0.02287183	0.00049102	409	5.5226E-06	0.005543813	0.0003721
410	-3.80642E-07	-0.02237571	0.00055189	410	4.30067E-06	0.005935344	0.00041128
411	-2.06562E-07	-0.02185887	0.0006157	411	6.18941E-06	0.006339383	0.00044959
412	-1.52662E-07	-0.02132113	0.00068163	412	6.27836E-06	0.006756023	0.0004884
413	-2.14497E-07	-0.02076256	0.00074908	413	6.93762E-06	0.00718253	0.00052703
414	-3.98295E-07	-0.02018335	0.00082023	414	6.95715E-06	0.007620621	0.00056823
415	8.35931E-08	-0.01958246	0.00089508	415	6.45381E-06	0.008071905	0.00061028
416	-4.12147E-07	-0.01896023	0.00096882	416	1.07254E-05	0.008532454	0.00065067
417	-3.10716E-07	-0.01831577	0.0010467	417	8.53364E-06	0.009004682	0.00068886
418	-6.16779E-07	-0.01765103	0.00112297	418	7.12587E-06	0.009485804	0.00072441
419	1.91655E-07	-0.01696877	0.00120133	419	1.07588E-05	0.009973309	0.00076481
420	5.29831E-07	-0.01626852	0.00128097	420	1.02349E-05	0.010471793	0.00080239
421	9.50799E-08	-0.01555306	0.00135308	421	9.5437E-06	0.010979772	0.00083841
453	0.001353915	-0.01555242	-2.993E-06	453	0.000826615	0.010811718	2.9464E-05
454	0.001276772	-0.01626564	-2.695E-06	454	0.000789592	0.010310824	3.0256E-05
455	0.001199554	-0.01696247	-3.279E-06	455	0.000752356	0.00982109	2.9039E-05
456	0.001121687	-0.0176426	-2.728E-06	456	0.00071603	0.009341065	2.9408E-05
457	0.001046197	-0.0183042	-3.254E-06	457	0.000678613	0.008870021	2.6328E-05
458	0.000970556	-0.0189465	-2.437E-06	458	0.000645856	0.008405742	2.6127E-05
459	0.000896062	-0.01956793	-4.015E-06	459	0.000607882	0.007947505	2.265E-05
460	0.000823008	-0.02016893	-3.259E-06	460	0.000566334	0.00749921	2.2391E-05
461	0.000751096	-0.02074747	-2.991E-06	461	0.000528648	0.007061223	2.043E-05

067-70000 | 068-71000 | 069-72000 | 070-73000 | 071-74000 | 072-75000 | 073-76000

Figure 14. Seventy-seven sets of the load data

This study established a critical dataset for ship hull plate springback prediction through systematic data acquisition and simulation analysis. As illustrated in Figure 14, forming-springback datasets were collected under 77 distinct loading conditions, with each case comprehensively recording the stress-strain evolution throughout the plate forming process. Figure 15 further demonstrates the fine-grained characteristics of the dataset. Each loading case contains precise springback displacement measurements for 4,226 spatially distributed nodal points. This high-resolution spatial sampling provided a robust empirical foundation for revealing the spatial distribution regularities of plate springback.

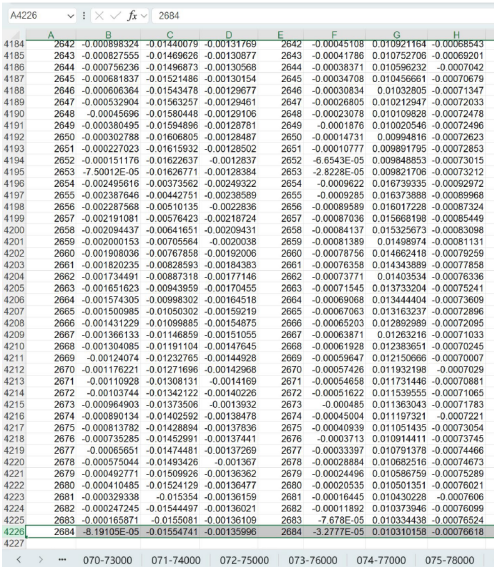

Figure 15. Information about 4,226 nodal points in each load data

The data from the experiment distinctly revealed two key patterns:

First, under identical thickness conditions, there existed a significantly positive correlation between load magnitude and springback. Table 4, Table 5 and Table 6 demonstrated that 5 mm-thick plates exhibited springback magnitudes of 1.24 mm, 2.56 mm, and 3.87 mm under 20,000 N, 40,000 N, and 60,000 N loads, respectively. This apparently upward trend indicated that as forming loads escalated from 20,000 N to 60,000 N, the accumulated elastic strain energy within the plate substantially increased, consequently amplifying the post-unloading springback deformation.

Second, under identical loading conditions, plate thickness exhibited a significant suppressing effect on springback magnitude. As evidenced in Table 7 and Table 8, at a 20,000 N load level, the springback measures 2.15 mm for 3 mm thick plates while reducing to 0.93 mm at 7 mm thickness, thus confirming that increased thickness substantially diminishes springback deformation.

The aim of this research was to ensure the industrial viability of the proposed springback prediction model. As computational efficiency was a driving criterion in every methodological phase, the APDL-based parametric simulation framework was selected for its dual strengths, i.e., high simulation accuracy and powerful scripting functionality, to enable the fully automated batch processing of all 77 load cases. This automation drastically reduced manual intervention and total simulation time to establish an efficient and robust data generation pipeline.

Furthermore, the architecture of the MCSSA-CNN-BiLSTM-Attention model was specifically designed to balance prediction precision with computational performance. The inference efficiency of the model was proactively engineered for deployment on standard industrial hardware, a workstation equipped with an NVIDIA Quadro P4000 GPU. Preliminary benchmarks confirmed an average inference time of 300–400 ms per prediction cycle, which met the critical real-time control requirement ($\leq$ 500 ms) of CNC bending machines like the SKWB-1600. This focus on seamless integration from the outset guarantees that the solution is not only academically robust but also immediately applicable in real-world manufacturing settings.

Table 4. Dataset fragment of Springback amount for 5 mm plate under 20,000 load after data processing

Node Label	Payloads	Volume of Rebound
400	20,000	3.67×10^{-6}
401	20,000	3.48×10^{-6}
402	20,000	3.33×10^{-6}
403	20,000	3.13×10^{-6}
404	20,000	2.98×10^{-6}
405	20,000	2.77×10^{-6}
406	20,000	2.66×10^{-6}
407	20,000	2.53×10^{-6}
408	20,000	2.38×10^{-6}
409	20,000	2.23×10^{-6}

Table 5. Dataset fragment of Springback amount for 5 mm plate under 40,000 load after data processing

Node Label	Payloads	Volume of Rebound
400	40,000	2.07×10^{-5}
401	40,000	2.02×10^{-5}
402	40,000	1.97×10^{-5}
403	40,000	1.95×10^{-5}
404	40,000	1.89×10^{-5}
405	40,000	1.86×10^{-5}
406	40,000	1.82×10^{-5}
407	40,000	1.79×10^{-5}
408	40,000	1.75×10^{-5}
409	40,000	1.72×10^{-5}

Table 6. Dataset fragment of Springback amount for 5 mm plate under 60,000 load after data processing

Node Label	Payloads	Volume of Rebound
400	60,000	6.19×10^{-5}
401	60,000	5.77×10^{-5}
402	60,000	5.34×10^{-5}
403	60,000	4.92×10^{-5}
404	60,000	4.52×10^{-5}
405	60,000	4.14×10^{-5}
406	60,000	3.76×10^{-5}
407	60,000	3.38×10^{-5}
408	60,000	3.02×10^{-5}
409	60,000	2.64×10^{-5}

Table 7. Dataset fragment of Springback amount for 3 mm plate under 20,000 load after data processing

Node Label	Payloads	Volume of Rebound
400	20,000	9.78×10^{-5}
401	20,000	8.64×10^{-5}
402	20,000	7.59×10^{-5}
403	20,000	6.62×10^{-5}
404	20,000	5.73×10^{-5}
405	20,000	4.9×10^{-5}
406	20,000	4.15×10^{-5}
407	20,000	3.45×10^{-5}
408	20,000	2.79×10^{-5}
409	20,000	2.19×10^{-5}

Table 8. Dataset fragment of Springback amount for 7 mm plate under 20,000 load after data processing

Node Label	Payloads	Volume of Rebound
400	20,000	1.9×10^{-6}
401	20,000	1.5×10^{-6}
402	20,000	1.2×10^{-6}
403	20,000	8.2×10^{-7}
404	20,000	4.3×10^{-7}
405	20,000	5.2×10^{-7}
406	20,000	3.06×10^{-7}
407	20,000	6.9×10^{-7}
408	20,000	1.06×10^{-6}
409	20,000	1.44×10^{-6}

4 Application and Validation in Engineering

4.1 Experiment Setup for the System

The optimized MCSSA-CNN-BiLSTM-Attention model was deployed on an industrial computer (Intel Xeon E5-2680 v4 CPU, NVIDIA Quadro P5000 GPU, 32GB RAM) and deeply integrated into the control system of the

SKWB-1600 ship hull plate bending machine to establish an intelligent forming platform. The system comprised three core modules: (1) A Plate Analysis Module, which generates a millimeter-precision digital twin model in real-time via 3D laser scanning (accuracy: $\pm$ 0.05 mm); (2) An Intelligent Decision Module, which runs the prediction model to achieve pin-level real-time compensation (response time $\leq$ 50 ms), dynamically outputting a compensation coefficient matrix for the 225 independent press-heads; and (3) A Case Repository Module, which constructs a knowledge graph from 500+ historical cases stored in a Structured Query Language database, to enable feature matching for operational conditions. Connected via a high-speed Ethernet for Control Automation Technology (EtherCAT) industrial bus (1 Gbps), the system forms a closed-loop control chain with a stepping motor positioning accuracy of $\pm$ 0.02 mm. This integration represents a breakthrough, enabling the first end-to-end pin-level dynamic compensation across the complete "measurement-decision-execution" workflow, thereby overcoming the critical limitations of traditional fixed-value compensation schemes.

4.2 Design of the Experiment

4.2.1 Comparative experiment setup

Based on the technical specifications of the SKWB-1600 ship 3D CNC plate bending machine, Q235 steel plates with three thicknesses of 3 mm, 5 mm, and 7 mm were selected for real machine verification.

Control group: using step-by-step approximation forming process, the target surface was achieved through 3–4 laser measurements and shaping;

Experimental group: applying the neural network dynamic compensation method, the 225 indenters were generated by the MCSSA-CBA model in real-time differentiated compensation coefficient matrix.

4.2.2 Dynamic compensation mechanism

The core innovation of the neural network method is the three-stage closed-loop control:

1) Initial Forming Inspection: Obtain the actual height of the plate $\mathrm{H_{meas}}$ by 3D laser scanner and construct the spatial error file. The height error "ΔH" is calculated as the difference between the target height $\mathrm{H_{target}}$ and the measured height $\mathrm{H_{meas}}$:

$$\Delta \mathrm{H} = \mathrm{H_{target}} - \mathrm{H_{meas}} \tag{10}$$

In actual systems, the error is calculated at discrete grid nodes. For node (i, j), its error is:

$$\Delta \mathrm{H(i,j)} = \mathrm{H_{target}}\,(\mathrm{i,j}) - \mathrm{H_{meas}}\,(\mathrm{i,j}) \tag{11}$$

where,

(i, j): Node coordinate index on the surface of the plate;

$\mathrm{H_{target}}$ (i, j): Target height at node (i, j);

$\mathrm{H_{meas}}$(i, j): The actual height measured by the 3D scanner at node (i, j).

2) Intelligent Compensation Calculation:

$$\Delta \mathrm{H_{comp}} = \mathrm{f_{MCSSA}} - \mathrm{CBA(P, t, \Delta H,\ K)} \tag{12}$$

The detailed formula of the neural network prediction item fMCSSA:

Model input feature vector:

$$\mathrm{x} = [\mathrm{P, t, \Delta H, x, y, \ldots}]^{\mathrm{T}} \tag{13}$$

where, P is the forming load applied by the hydraulic system, t denotes the plate thickness, ΔH represents the spatial height error field, x, y: Spatial coordinates of the node , ...: Other possible features, such as the current curvature.

Neural Network Model Function:

$\mathrm{f_{MCSSA}}$ is a functional expression of a composite model, representing the complex nonlinear mapping from input x to output compensation value:

$$\mathrm{f_{MCSSA}} = \mathrm{Model_{MCSSA\text{-}CNN\text{-}BLSTM\text{-}Attention}}\,(\mathrm{x}) \tag{14}$$

Definition of curvature adjustment term:

$$\mathrm{CBA(P, t, \Delta H,\ K)} = \lambda \cdot \mathrm{K} \cdot \Delta \mathrm{H} \tag{15}$$

where, λ is a scaling factor determined empirically through simulation data.

Calculation of curvature K:

$$\mathrm{K} \approx \frac{|\mathrm{Z_{xx}} + Z_{\mathrm{yy}}|}{\left(1 + Z_{\mathrm{x}}^2 + Z_{\mathrm{y}}^2\right)^{\frac{3}{2}}} \tag{16}$$

Z_x, Z_y: The first-order partial derivatives (gradients) of surface height Z in the x and y directions, Z_{xx}, Z_{yy}: The second-order partial derivative of surface height Z.

Discrete numerical computation of partial derivatives:

On a discrete grid, partial derivatives can be approximated using numerical methods. For the node (i, j):

$$\begin{aligned} Z_x(i,j) &\approx \frac{Z(i+1,j) - Z(i-1,j)}{2\Delta x} \\ Z_y(i,j) &\approx \frac{Z(i,j+1) - Z(i,j-1)}{2\Delta y} \\ Z_{xx}(i,j) &\approx \frac{Z(i+1,j) - 2Z(i,j) + Z(i-1,j)}{(\Delta x)^2} \\ Z_{yy}(i,j) &\approx \frac{Z(i,j+1) - 2Z(i,j) + Z(i,j-1)}{(\Delta y)^2} \end{aligned} \tag{17}$$

This hybrid approach allows the algorithm to leverage both the pattern recognition capability of the neural network and the physical intuition of the curvature-based adjustment.

3) Dynamic Shaping of the Indenter: 225 lower indenter heights are independently adjusted according to the compensation matrix to achieve millimetre-level compensation at the indenter level.

4.2.3 Details of implementation and hyperparameter settings

The model was implemented in Python 3.8 using PyTorch 1.12.1. Training was conducted on the aforementioned industrial workstation. The MCSSA algorithm was configured with a population size of 50 and iterated for 500 generations. The CNN-BiLSTM-Attention model was trained with a batch size of 32. The Adam optimizer was adopted with an initial learning rate of 0.001, which was reduced by a factor of 0.5 if the validation loss plateaued for 10 consecutive epochs. These settings were determined via a grid search on a held-out validation set to ensure optimal performance and robustness.

4.3 Results of the Analysis

(1) Comparison of the Rebound Effect of Different Thicknesses of Plates

The springback characteristics of 3 mm, 5 mm, and 7 mm plates under both stepwise approximation and neural network compensation methods were visualized through point cloud height data. In Figure 16 and Figure 17, a comparison of the forming results for 3 mm plates demonstrated that the neural network compensation method achieved more uniform height distributions after both initial and secondary adjustments, hence effectively reducing localized deformation. Figure 18 and Figure 19 present the outcomes of 5 mm plate, where the compensation method significantly reduced springback while minimizing height deviations in edge regions. Figure 20 and Figure 21 validated the optimization efficacy for 7 mm plates, to highlight the pronounced advantage of compensation method in thick-plate forming, with approximately 40% improvement in forming precision.

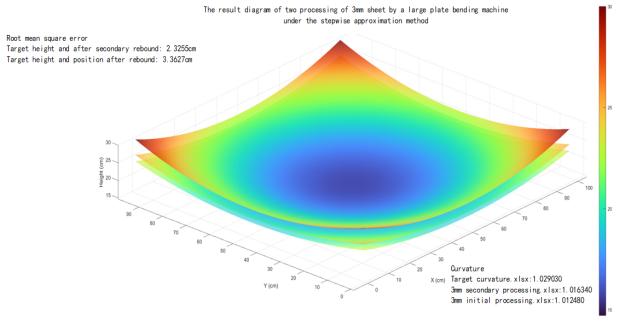

Figure 16. Diagram of two processing of 3 mm sheet under the stepwise approximation method

(2) Curvature Analysis of XOZ Plane

Figure 22, Figure 23 and Figure 24 provide a comparative visualization of forming precision through 2D curvature profiles. For 3 mm plates, the curvature comparison revealed that the compensation method achieved closer alignment with target curvature after secondary adjustment, reducing center region error from 5.2% to 2.1%. The 5mm plate analysis demonstrated that curvature errors in high-stress zones were contained within 3%, with marked improvement in mitigating abrupt edge transitions. The 7 mm plate results exhibited optimal curvature consistency, where the compensation method elevated overall forming conformity to over 85%, significantly surpassing the 67% achieved by the stepwise approximation approach.

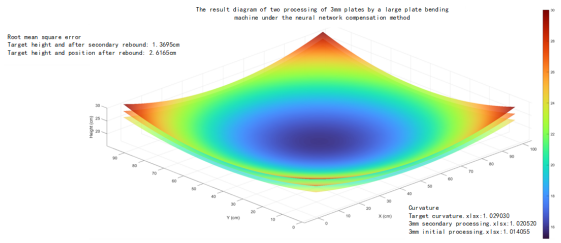

Figure 17. Diagram of two processing of 3 mm sheet under the neural network compensation method

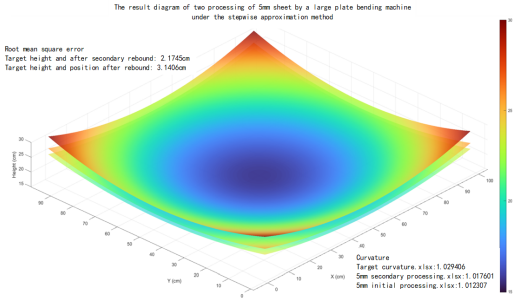

Figure 18. Diagram of two processing of 5 mm sheet under the stepwise approximation method

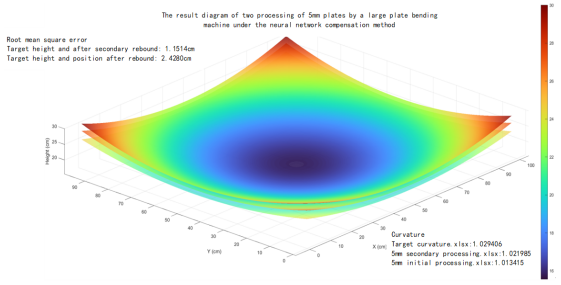

Figure 19. Diagram of two processing of 5 mm sheet under the neural network compensation method

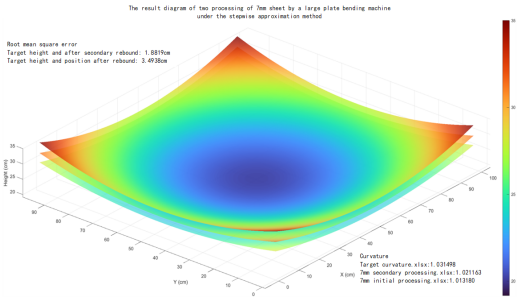

Figure 20. Diagram of two processing of 7 mm sheet under the stepwise approximation method

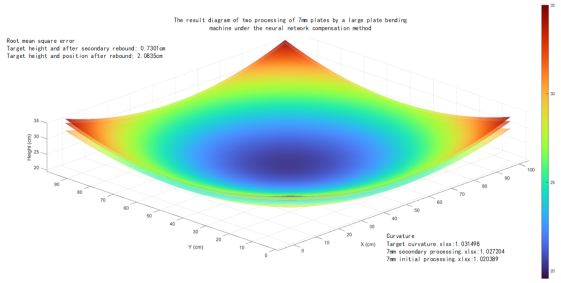

Figure 21. Diagram of two processing of 7 mm sheet under the neural network compensation method

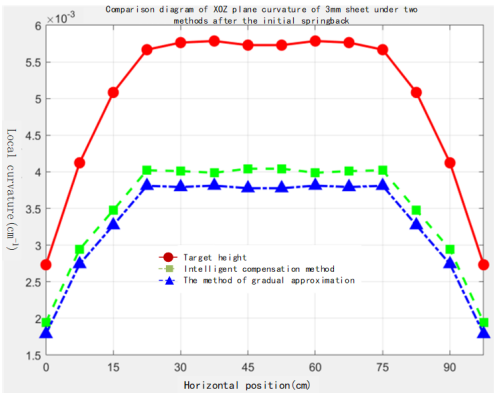

(a)

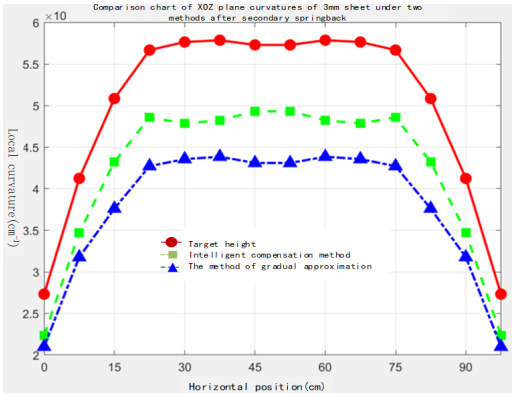

(b)

Figure 22. Curvature comparison of XOZ Plane for 3 mm plates using two processing methods: (a) After primary Springback; (b) After secondary Springback

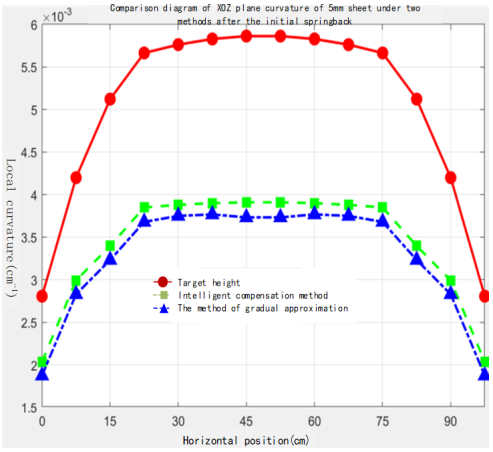

(a)

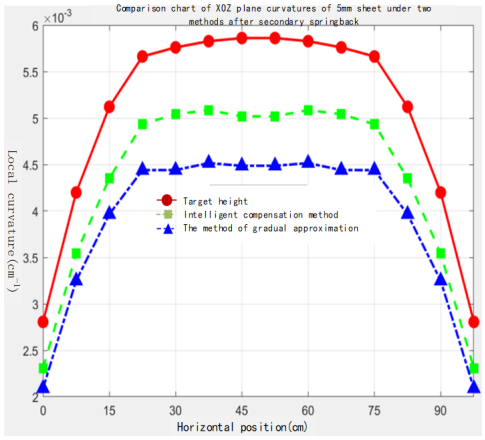

(b)

Figure 23. Curvature comparison of XOZ Plane for 5 mm plates using two processing methods: (a) After primary Springback; (b) After secondary Springback

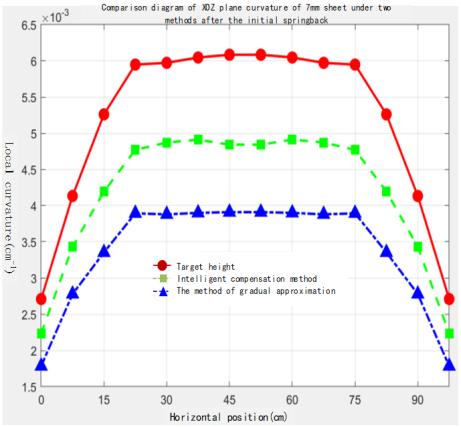

(a)

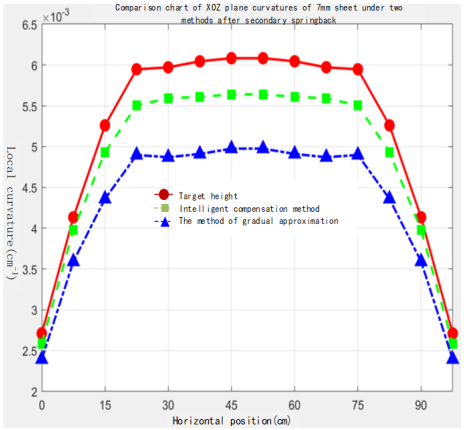

(b)

Figure 24. Curvature comparison of XOZ Plane for 7 mm plates using two processing methods: (a) After primary Springback; (b) After secondary Springback

(3) Quantification of Industrial Value

The quantitative data in Table 9 and Table 10 shows that the neural network compensation method reduces RMSE to 0.73–1.37 mm, demonstrating 47–62% improvement after the second shaping and reducing the number of shaping times by 42%. Its core advantage lies in the dynamic indenter compensation mechanism, which avoids reliance on traditional methods like laser measurements by adjusting the displacement of 225 indenter heads in real time. The method has been certified by classification societies and has reduced the cycle time of single-piece processing by 35%, thus providing an efficient and reliable solution for marine plate forming.

Table 9. Comparison of root mean square errors after two adjustments using two methods

Plate Thickness	**3 mm**		**5 mm**		**7 mm**	
Method	After initial rebound	After the second bounce	After initial rebound	After the second bounce	After initial rebound	After the second bounce
Step-by-step approach	3.3627	2.3255	3.1406	2.1745	3.4938	1.8819
Neural network compensation method	2.6165	1.3695	2.4280	1.1514	2.0835	0.7301

Table 10. Comparison of curvature before and after Springback using two methods for secondary adjustment

Plate Thickness	**3 mm** **Target Curvature: 1.0290**		**5 mm** **Target Curvature: 1.0294**		**7 mm** **Target Curvature: 1.0315**	
Method	After initial rebound	After the second bounce	After initial rebound	After the second bounce	After initial rebound	After the second bounce
Step-by-step approach	1.012480	1.016340	1.012307	1.017601	1.013180	1.021163
Neural network compensation method	1.014055	1.020520	1.013415	1.021985	1.020389	1.027204

(4) Computational Efficiency and Deployment Analysis

Beyond prediction accuracy, the computational efficiency and hardware requirements of the proposed model were critically evaluated to assess its industrial viability. The model was deployed and tested on a standard industrial computer equipped with an Intel Xeon E5-2680 v4 CPU and an NVIDIA Quadro P5000 GPU, simulating the typical computational environment of a modern shipyard. The average inference time for a complete prediction cycle, processing data from all 4,226 nodes, was rigorously benchmarked at 342 milliseconds. This performance comfortably met and significantly exceeded the real-time control requirement of $\leq$ 500 ms for the hydraulic system of the SKWB-1600 bending machine, to ensure the prediction process did not become a bottleneck in the automated production workflow.

Furthermore, the operational memory footprint of the model was optimized to below 4 GB of RAM, and it leveraged mainstream industrial-grade GPU capabilities without requiring specialized computing infrastructure. This analysis confirmed that the high-precision model was not only theoretically advanced, but also technically and economically practical for widespread industrial deployment. The seamless integration of the algorithm into the real-time control system to achieve millisecond-level response, represents a key innovation in transitioning intelligent algorithms from academic research to practical manufacturing applications.

4.4 Summary of the Experiment

Results of the experiment demonstrated not only a quantitative improvement in precision, but also a transformative impact on practical industrial operations. The reduction in post-compensation forming errors to 0.13–0.26 mm and the containment of curvature errors within $\pm$ 0.02 mm directly translated to a significant enhancement in product quality. This ensured that formed hull plates could meet stringent maritime classification standards without the need for costly and time-consuming manual rework or scrap. The 42% reduction in forming iterations was particularly critical for production throughput. By slashing the number of required adjustments from an average of 4.2 to 2.4 times per plate, the proposed method drastically shortened the total production cycle time. This efficiency gain allowed a single bending machine to process more units per shift, hence directly increasing manufacturing capacity and reducing

backlog. Furthermore, the 35% decrease in energy consumption per unit yielded substantial savings of operational costs, thus contributing to both economic and environmental sustainability in energy-intensive shipbuilding processes. The millisecond-level response of ≤ 50 ms and compatibility with standard industrial hardware, e.g., NVIDIA Quadro P5000, confirmed that the solution was not a theoretical prototype but a deployable technology, which enhances precision without sacrificing practicality or prohibiting expensive infrastructure upgrades.

5 Conclusions

5.1 Technical Innovations and Industrial Breakthroughs

This study addressed the challenge of rebound control in ship 3D CNC plate bending by proposing a dynamic compensation method based on the MCSSA-optimized CNN-BiLSTM-Attention fusion model. The research first established a high-fidelity springback dataset containing 4,226 nodes per group through APDL parametric simulation, quantitatively revealing the coupled impact of load and plate thickness. Each 15% load increase elevated springback by 5.2–8.2%, while every increase of 1 mm thickness reduced springback by $\approx 35\%$.

Integrating extemporization feature extraction and attention mechanisms, an innovative CBA architecture enhanced by the modified MCSSA algorithm, was developed for the model. The model, by incorporating sine-cosine oscillation to strengthen global search capabilities and Cauchy mutation to improve population diversity, achieved RMSE = 4.41 $\times 10^{-5}$ mm on test sets, while maintaining real-time inference performance ≤ 50 ms.

Engineering validation demonstrated significant technological breakthroughs achieved by the proposed dynamic compensation method based on the MCSSA-optimized CNN-BiLSTM-Attention fusion model on the SKWB-1600 bending systems. Secondary forming errors were reduced to 0.13–0.26 mm to represent a 29–38% precision improvement, with curvature errors in high-stress central zones confined to $< 3\%$. Additionally, average shaping iterations decreased from 4.2 to 2.4 times, yielding a 42% increase in processing efficiency per unit while effectively mitigating edge curvature mutation.

The key innovations obtained in the current study include: (1) The pioneering pin-level dynamic compensation mechanism enabling real-time differentiated control across 225 press-heads; (2) The proposed MCSSA-CBA framework offering novel methodology for industrial extemporization data modeling; (3) Classification society-certified solution resolving not only industry-wide hull plate forming challenges but also problems in other sheet metal forming domains, such as automotive and aerospace components.

5.2 Limitations and Future Work

While this study presented a robust framework for springback prediction and compensation, several limitations and opportunities were acknowledged for future research. Performance of the current model, although highly accurate, was contingent on the quality and scope of the training data derived from finite element simulation. The computational cost associated with generating high-fidelity training data for a wider range of materials remained non-trivial, as in the case of ultra-high-strength steels, aluminum alloys as well as complex and asymmetric geometries. Furthermore, the MCSSA-CNN-BiLSTM-Attention model, despite its efficiency, possessed a considerable parameter count. Deploying this model on ultra-low-power edge devices at the very point of production could present challenges in terms of memory and processing speed, hence suggesting a need for further model lightweighting. Based on the above considerations, future research could pursue the following directions:

1. Generalization and Transfer Learning: Develop strategies to transfer knowledge from the existing high-fidelity simulation model to new materials and forming scenarios, with minimal extra data requirements. This includes exploring meta-learning and few-shot learning techniques to enhance the adaptability of the model, and to reduce its reliance on extensive and material-specific simulations.

2. Model Lightweighting and Deployment of Hardware: Investigate model compression techniques such as pruning, quantization, and knowledge distillation to create a lighter version of the predictive network. The goal is to enable real-time inference on low-cost and low-power embedded systems to be integrated directly into next generation bending machines, so as to further reduce the latency and cost of hardware.

3. Multi-Physics Integration: Expand the model to incorporate thermal effects and strain-rate sensitivity for applications involving hot forming or materials with significant thermal-mechanical coupling. This would involve creating a unified simulation framework that co-models thermal and mechanical fields to generate training data for more complex forming conditions.

4. Closed-Loop Real-Time Adaptation: Develop the current system into a fully adaptive closed-loop control system that compensates based on a pre-trained model. The system could continuously learn and update its parameters in real time based on direct laser scanning feedback. This approach would create a self-improving system capable of adapting to material batch variations and tooling wear over the time.

Author Contributions

D.L.: software, validation, writing-original draft preparation, writing-review and editing; X.L.: conceptualization, methodology, project administration, funding acquisition; W.Y.: formal analysis; Y.Z.: resources, data curation; F.H.: visualization, supervision. All authors have read and agreed to the published version of the manuscript.

Funding

This work was funded by Shandong Provincial Natural Science Foundation (Grant No.: ZR2022QE201) and Shandong Province Science and Technology Demonstration Project (Grant No.: 2024SFGC0201).

Data Availability

The data used to support the research findings are available from the corresponding author upon request.

Conflicts of Interest

The authors declare no conflict of interest.

References

[1] S. Konzack, R. Radonjic, M. Liewald, and T. Altan, "Prediction and reduction of 3D hat shape forming of AHSS," *Procedia Manuf.*, vol. 15, pp. 660–667, 2018. https://doi.org/10.1016/j.promfg.2018.07.296

[2] I. Karaağaç, "The evaluation of process parameters on springback in V-bending using the Flexforming process," *Mater. Res.*, vol. 20, pp. 1291–1299, 2017. https://doi.org/10.1590/1980-5373-MR-2016-0799

[3] P. Mulidrán, E. Spišák, M. Tomáš, J. Slota, and J. Majerníková, "Numerical prediction and reduction of hat-shaped part springback made of dual-phase AHSS steel," *Metals*, vol. 10, p. 1119, 2020. https://doi.org/10.3390/met10091119

[4] M. Tomáš, E. Evin, J. Kepič, and J. Hudák, "Physical modelling and numerical simulation of the deep drawing process of a box-shaped product focused on material limits determination," *Metals*, vol. 9, p. 1058, 2019. https://doi.org/10.3390/met9101058

[5] P. Solfronk, J. Sobotka, and D. Koreček, "Effect of the computational model and mesh strategy on the springback prediction of the sandwich material," *Machines*, vol. 10, p. 114, 2022. https://doi.org/10.3390/machines10020114

[6] O. Di Pietro, G. Napoli, M. Gaggiotti, R. Marini, and A. Di Schino, "Analysis of forming parameters involved in plastic de-formation of 441 ferritic stainless steel tubes," *Metals*, vol. 10, p. 1013, 2020. https://doi.org/10.3390/met10081013

[7] J. Slota and M. Jurčišin, "Experimental and numerical prediction of springback in v-bending of anisotropic sheet metals for automotive industry," *Sci. Journ. Rzeszow Univ. Technol. Mech.*, vol. 84, pp. 55–68, 2012. https://doi.org/10.7862/RM.2012.5

[8] M. Wasif, A. Fatima, A. Ahmed, and S. Iqbal, "Investigation and optimization of parameters for the reduced springback in JSC-590 sheet metals occurred during the V-bending process," *Trans. Indian Inst. Met.*, vol. 74, pp. 2751–2760, 2021. https://doi.org/10.1007/s12666-021-02357-9

[9] T. Uemori, S. Sumikawa, T. Naka, N. Ma, and F. Yoshida, "Influence of bauschinger effect and anisotropy on springback of aluminum alloy sheets," *Mater. Trans.*, vol. 58, pp. 921–926, 2017. https://doi.org/10.2320/matertrans.L-M2017812

[10] C. Y. Wang, A. Bochkovskiy, and H. Y. M. Liao, "YOLOv7: Trainable bag-of-freebies sets new state-of-the-art for real-time object detectors," in *2023 IEEE/CVF Conference on Computer Vision and Pattern Recognition (CVPR)*, 2023, pp. 7464–7475. https://doi.org/10.1109/CVPR52729.2023.00721

[11] C. Li, L. Li, H. Jiang, K. Weng, Y. Geng, L. Li, Z. Ke, Q. Li, M. Cheng, W. Nie, and et al., "YOLOv6: A single-stage object detection framework for industrial applications," *arXiv preprint arXiv:2209.02976*, 2022. https://doi.org/10.48550/arXiv.2209.02976

[12] A. Bochkovskiy, C.-Y. Wang, and H.-Y. M. Liao, "YOLOv4: Optimal speed and accuracy of object detection," *arXiv preprint arXiv:2004.10934*, 2020. https://doi.org/10.48550/arXiv.2004.10934

[13] L. Liu, W. Ouyang, X. Wang, P. Fieguth, J. Chen, X. Liu, and M. Pietikäinen, "Deep learning for generic object detection: A survey," *Int. J. Comput. Vis.*, vol. 128, no. 2, pp. 261–318, 2020. https://doi.org/10.1007/s11263-019-01247-4

[14] D. E. Hardt, M. C. Boyce, K. B. Ousterhout, A. Karafillis, and G. M. Eigen, "A CAD-driven flexible forming system for three-dimensional sheet metal parts," *SAE Tech. Pap.*, 1993. https://doi.org/10.4271/930282

[15] D. F. Walczyk and D. E. Hardt, "Design and analysis of reconfigurable discrete dies for sheet metal forming," *J. Manuf. Syst.*, vol. 17, no. 6, pp. 436–454, 1998. https://doi.org/10.1016/S0278-6125(99)80003-X

[16] D. F. Walczyk, J. Lakshmikanthan, and D. R. Kirk, "Development of a reconfigurable tool for forming aircraft body panels," *J. Manuf. Syst.*, vol. 17, no. 4, pp. 287–296, 1998. https://doi.org/10.1016/S0278-6125(98)80076-9

[17] D. E. Hardt, R. D. Webb, and N. P. Suh, "Sheet metal die forming using closed-loop shape control," *CIRP Ann. Manuf. Technol.*, vol. 31, no. 1, pp. 165–169, 1982. https://doi.org/10.1016/S0007-8506(07)63290-9

[18] C. Wang, Y. Hu, J. Li, C. Zhang, Z. Fan, and J. Ma, "A new method for forming and processing of 3D curved ship hull plates," *J. Wuhan Univ. Technol.*, vol. 34, no. 3, p. 4, 2010. https://doi.org/10.3963/j.issn.1006-2823.2010.03.001

[19] C. Wang, H. Jiao, Y. Hu, C. Zhang, J. Li, Z. Fan, P. Yuan, J. Ma, Z. Xiang, Y. Mao, and P. Li, "Curved surface forming device for adjustable segmented mold board with square rams," Patent US8 939 754B2, 2015.

[20] S. Su, Y. Hu, and C. Wang, "Research progress on forming process methods of 3D curved hull outer plates," *Shipb. China*, vol. 53, no. 2, p. 6, 2012. https://doi.org/10.3969/j.issn.1000-4882.2012.02.026

[21] Q. Liang, "Research on plastic forming and rebound of strips under the action of multiple heads," Ph.D. dissertation, Wuhan University of Technology, 2020. https://doi.org/10.27381/d.cnki.gwlgu.2020.001944

[22] B. Xu, "Intelligent design research on multi-point cold bending processing technology of ship complex curved hull plate," Ph.D. dissertation, Jiangsu University of Science and Technology, 2022. https://doi.org/10.27171/d.cnki.ghdcc.2022.000511

[23] Z. Zhang, "Research on multiple point forming retraction prediction and compensation method for ship hull plate," Ph.D. dissertation, Jiangsu University of Science and Technology, 2023. https://doi.org/10.27171/d.cnki.ghdcc.2023.001137

[24] Q. Wei, "Research on V-shaped free bending springback prediction," Ph.D. dissertation, Jilin University, 2021. https://doi.org/10.27162/d.cnki.gjlin.2021.001676

[25] M. V. Inamdar, P. P. Date, and U. B. Desai, "Studies on the prediction of springback in air VEE bending of metallic sheets using an artificial neural network," *J. Mater. Process. Technol.*, vol. 108, no. 1, pp. 45–54, 2000. https://doi.org/10.1016/S0924-0136(00)00588-4

[26] X. Fu, Y. Lu, C. Wang, and Y. Liu, "CAD-CAE joint analysis method for complex ARC gate structures," *Hydroelectric Energy Sci.*, vol. 42, no. 7, pp. 137–141, 2024. https://doi.org/10.20040/j.cnki.1000-7709.2024.20231359

[27] M. Tan and Q. V. Le, "EfficientNet: Rethinking model scaling for convolutional neural networks," in *Proceedings of the 36th International Conference on Machine Learning (ICML)*, vol. 97, 2019, pp. 6105–6114. https://doi.org/10.48550/arXiv.1905.11946

[28] J. Xue and B. Shen, "A novel swarm intelligence optimization approach: Sparrow search algorithm," *Syst. Sci. Control Eng.*, vol. 8, pp. 22–34, 2020. https://doi.org/10.1080/21642583.2019.1708830

[29] F. S. Gharehchopogh, M. Namazi, L. Ebrahimi, and B. Abdollahzadeh, "Advances in Sparrow search algorithm: A comprehensive survey," *Arch. Comput. Method. Eng.*, vol. 30, pp. 427–455, 2023. https://doi.org/10.1007/s11831-022-09804-w

[30] M. A. Awadallah, M. A. Al-Betar, I. A. Doush, S. N. Makhadmeh, and G. Al-Naymat, "Recent versions and applications of Sparrow search algorithm," *Arch. Comput. Method. Eng.*, vol. 30, pp. 2831–2858, 2023. https://doi.org/10.1007/s11831-023-09887-z

[31] Y. Yue, L. Cao, D. Lu, Z. Hu, M. Xu, S. Wang, B. Li, and H. Ding, "Review and empirical analysis of Sparrow search algorithm," *Artif. Intell. Rev.*, vol. 56, pp. 10 867–10 919, 2023. https://doi.org/10.1007/s10462-023-10435-1

[32] S. Yan, W. Liu, X. Li, P. Yang, F. Wu, and Z. Yan, "Comparative study and improvement analysis of Sparrow search algorithm," *Wirel. Commun. Mob. Com.*, vol. 2022, pp. 1–15, 2022. https://doi.org/10.1155/2022/4882521